

We are IntechOpen, the world's leading publisher of Open Access books Built by scientists, for scientists

6,900

Open access books available

186,000

International authors and editors

200M

Downloads

Our authors are among the

154

Countries delivered to

TOP 1%

most cited scientists

12.2%

Contributors from top 500 universities



WEB OF SCIENCE™

Selection of our books indexed in the Book Citation Index
in Web of Science™ Core Collection (BKCI)

Interested in publishing with us?
Contact book.department@intechopen.com

Numbers displayed above are based on latest data collected.
For more information visit www.intechopen.com



Surface Magneto Plasmons and Their Applications

Bin Hu

Additional information is available at the end of the chapter

<http://dx.doi.org/10.5772/intechopen.79788>

Abstract

Due to their promising properties, surface magneto plasmons have attracted great interests in the field of plasmonics. Apart from flexible modulation of the plasmonic properties by an external magnetic field, surface magneto plasmons also promise nonreciprocal effect and multi-bands of propagation, which can be applied into the design of integrated plasmonic devices for biosensing and telecommunication applications. In the visible frequencies, hybrid nanodevices consisting of metals and magnetic materials based on surface magneto plasmon are proposed. In the infrared frequencies, highly-doped semiconductors can replace metals, owing to the lower incident wave frequencies and lower plasma frequencies. Furthermore, a promising 2D material-graphene shows great potential in infrared magnetic plasmonics. In this book chapter, we will review the magneto plasmonics with a focus on device designs and applications. We will give the basic theory of surface magneto plasmons propagating in different structures, including plane surface structures and slot waveguides. Based on the fundamental investigation and theoretical studies, we will illustrate various magneto plasmonic micro/nanodevices, such as tunable waveguides, filters, and beam-splitters. Novel plasmonic devices such as one-way waveguides and broad-band waveguides will also be introduced.

Keywords: surface magneto plasmons, plasmonics, magnetic field tuning

1. Introduction

Surface plasmons (SPs) are electromagnetic waves that are confined on and propagate along the surface of a conductor, usually a metal or a semiconductor [1]. SPs are caused by the resonant oscillation of the free electrons in the conductor with the incident electromagnetic waves. The resonant oscillation can be denoted by a characteristic frequency—the plasma frequency ω_p , which decides the scale of the free electrons response to time-varying perturbations [2]. Since SPs depend on the free electron motions, it can be imagined that an external

magnetic field may have modulations on the SPs, due to the Lorentz force which can change the response of carriers. In this situation, another characteristic frequency called cyclotron frequency ω_c is often used, which is a function of the effective mass of the charge carriers and the strength of the applied magnetic field [3]. One of the important consequences of magnetizing the plasmons is that the polarizability becomes highly anisotropic (the permittivity of the conductor becomes a tensor)—even though the medium is isotropic when the magnetic field is not applied. Therefore, SPs may have different properties when they are propagating under an external magnetic field. In this situation, they are usually called surface magneto plasmons (SMPs) [4].

SMPs can be divided in three principal configurations, according to three directions—the orientation of applied magnetic field \mathbf{B} , the propagation of the surface wave \mathbf{k} , and the surface. The first one is called perpendicular geometry, in which \mathbf{B} is perpendicular to both the surface and \mathbf{k} . The second one is called Faraday geometry, in which \mathbf{B} is parallel to the surface and \mathbf{k} . The third one is called Voigt geometry, in which \mathbf{B} is parallel to the surface and perpendicular to \mathbf{k} . Compared with traditional SPs, SMPs have several unique properties. For instance, SMPs in perpendicular geometry and Faraday geometry can support pseudo-surface waves, which means they attenuate on only one side of the surface [5, 6]. SMPs in this Voigt configuration support nonreciprocal effect, which means the SMP dispersions are different when they propagate along two opposite directions. In addition, unlike SPs only has one propagating frequency band which is below the plasma frequency [2], SMPs support two propagating bands.

The basic theory of SMPs in the perpendicular configuration was first given by Brion et al. [5] in 1974. Then, in the same year, Wallis et al. reported the theoretical study of SMPs in the Faraday configuration [6]. In 1987, Kushwaha [7] gave the theoretical derivation of SMP on a thin film in the Faraday configurations. For the Voigt configuration, the pioneer work was implemented by Chiu et al. [8] and Brion et al. [4] as early as 1972, separately. Then De Wames and coworkers studied the dispersion relation of Voigt-configured SMPs on a thin film [9]. Then SMP properties considering holes [10], optical phonons [11–13], diffuse electron density profiles [14], and metal screen [15] were theoretically proposed. They were also studied both theoretically and experimentally in various structures [16–27]. In 2001, a review work of SMP was given [28].

In recent years, due to the extraordinary optical transmission through periodic holds in nanometer scale, which is found in 1998 [29], numerous plasmonic devices, made of metals, have been theoretically proposed and experimentally realized in the visible frequencies [1, 30]. Compared with studies about SPs before 2000 [31–40], these structures have been mostly focused on the subwavelength confinement of electromagnetic waves [41]. For example, in the slot waveguides [42] or metal-insulator-metal structures [43], electromagnetic waves can be confined in a space as small as $\sim 0.1\lambda$. Inspired by these structures, some SMP devices composed of metals were proposed [44–49]. However, all of these SMP structures are difficult to realize because they require unreachable magnetic fields. The reason is that in order to observe the effect of an external magnetic field, it requires ω_p , ω_c and the incident angular frequency ω be comparable. However, for a metal in the visible frequencies, ω_p and ω are usually in the order of $\sim 10^{16}$ and $\sim 10^{15}$ Hz, respectively. Therefore, it needs a magnetic field as strong

as $\sim 10^3$ Tesla, which is difficult to realize in laboratories. So far, there are two ways to solve this problem. One is using ferromagnetic materials, such as Ni and Co in nanostructures [50–57]. By this method, the intensity of the applied magnetic field can be decreased to a scale of \sim mT. But it introduces large loss. The other solution is using semiconductors instead of metals in THz regime to decrease both ω_p and ω . ω_p of a doped semiconductor can be decreased in an order of $\sim 10^{13}$ Hz. Therefore, the required external magnetic field can be less than 2 Tesla. Some researches of SMP devices consisting of semiconductors have also been proposed recently [58–62].

In this chapter, we will introduce the basic theory of SMPs in the Voigt configuration and their applications in SMP devices design. In Section 2, we will give the dispersions of SMPs on a surface, in a metal-insulator-semiconductor structure, and in a semiconductor-insulator-semiconductor structure of the Voigt configuration. The nonreciprocal effect and the two propagating bands will be discussed. In Section 3, some intriguing plasmonic devices based on the SMPs will be presented, including one-way waveguides, broadly tunable THz slow light waveguides, and focal-length-tunable plasmonic lenses.

2. Theory of SMPs on a surface and in a slot waveguide

The first theory of SMPs on a conductor plane surface in the Voigt configuration was presented by Chiu et al. [8]. However, they only found the nonreciprocal effect. In the same year, Brion et al. gave a more comprehensive study on SMPs, including the nonreciprocal effect and the two propagating bands [4]. They also gave an explanation of why the higher band appears. We will give a review of his research in this section. Although the energy of SMPs is confined on the plane surface, the confinement is not subwavelength scale (in the order of $\sim 2-3\lambda$). In order to solve this problem, in this section, we derive the dispersion of SMPs in a slot waveguide, which can confine light in $1/10 \lambda$ in the lateral direction [63–66]. Some results are very similar with that in Ref. [4], while some are quite different. For example, the nonreciprocal effect is eliminated in a symmetric structure [63].

2.1. Dispersion of SMPs on a plane surface

The schematic structure is shown in **Figure 1**. The material of $x < 0$ is a metal or a semiconductor, and its surface is oriented to $+x$ -axis. The SMPs is propagating along the z -axis. In the Voigt configuration, the applied magnetic field \mathbf{B} is applied along the y -axis. Then the permittivity of the metal/semiconductor becomes a tensor:

$$\varepsilon = \begin{bmatrix} \varepsilon_{xx} & 0 & \varepsilon_{xz} \\ 0 & \varepsilon_{yy} & 0 \\ -\varepsilon_{xz} & 0 & \varepsilon_{xx} \end{bmatrix}. \quad (1)$$

The parameters in Eq. (1) have the expressions of

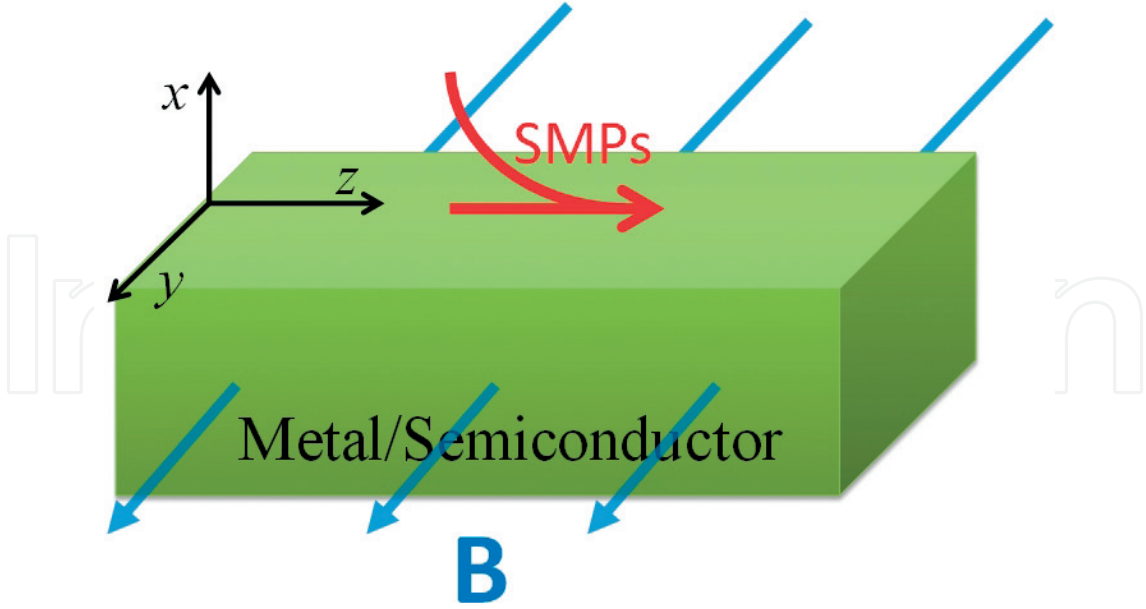


Figure 1. Schematic structure of SMPs propagating on a metal/semiconductor surface in the Voigt configuration. The external static magnetic field B is applied along the y -axis.

$$\varepsilon_{xx} = \varepsilon_{\infty} \left\{ 1 - \frac{\omega_p^2(\omega + iv)}{\omega[(\omega + iv)^2 - \omega_c^2]} \right\} \quad (2)$$

$$\varepsilon_{xz} = -i\varepsilon_{\infty} \frac{\omega_p^2\omega_c^2}{\omega[(\omega + iv)^2 - \omega_c^2]} \quad (3)$$

$$\varepsilon_{yy} = \varepsilon_{\infty} \left[1 - \frac{\omega_p^2}{\omega(\omega + iv)} \right] \quad (4)$$

in which ω_p is the plasma frequency of the conductor, ω is the angular frequency of the incident wave, ε_{∞} is the high-frequency permittivity, and $\omega_c = eB/m^*$ is the cyclotron frequency. e and m^* are the charge and the effective mass of electrons, respectively. B is the applied external magnetic field. $v = e/(\mu m^*)$ is the collision frequency of free electrons, μ is the carrier mobility.

From the Maxwell equations, the wave equation can be derived as

$$\nabla \times (\nabla \times \mathbf{E}) - k_0^2 \varepsilon \mathbf{E} = 0 \quad (5)$$

where k_0 is the wave vector in vacuum. ε is the permittivity of the material (for a conductor, it is the dielectric constant tensor of Eq. (1)). c is the light velocity in vacuum. If we assume that the material of the region $x > 0$ is a dielectric with permittivity of ε_d , and considering SMPs are TM polarized (with the magnetic field component parallel to the y -axis), the electromagnetic fields in the metal/semiconductor and the dielectric have the form:

$$\mathbf{E} = (E_{1x}, 0, E_{1z})e^{\alpha_0 x} e^{i(\beta z - \omega t)}, x \geq 0 \quad (6)$$

$$\mathbf{E} = (E_x, 0, E_z)e^{\alpha x} e^{i(\beta z - \omega t)}, x < 0 \quad (7)$$

where β is the wave vector of SMPs. From Eqs. (6), (7) and (1), we have a nontrivial solution of Eq. (5) only if

$$\alpha_0^2 = \beta^2 - \frac{\omega^2}{c^2} \varepsilon_d \quad (8)$$

$$\alpha^2 = \beta^2 - \frac{\omega^2}{c^2} \varepsilon_V \quad (9)$$

where $\varepsilon_V = \varepsilon_{xx} + \varepsilon_{xz}^2/\varepsilon_{xx}$ is the Voigt dielectric constant. With the consideration of the characteristics of the surface mode and the continuity of H_y and E_z at the surface, the dispersion relation of the waveguide is given by

$$\varepsilon_d \sqrt{\beta^2 - \frac{\omega^2}{c^2} \varepsilon_V} + \varepsilon_V \sqrt{\beta^2 - \frac{\omega^2}{c^2} \varepsilon_d} + i\beta \varepsilon_d \frac{\varepsilon_{xz}}{\varepsilon_{xx}} = 0. \quad (10)$$

It can be clearly seen from Eq. (10) that this dispersion is non-reciprocal with respect to the direction of propagation, i.e., the positive and negative values of the wave vector β are not equivalent. The dispersion equation can be solved numerically by Eq. (10). In **Figure 2**, the dispersion of SMPs on a plane surface is plotted, assuming that the conductor material is InSb in the lossless case ($\nu = 0$) with $\omega_c = 0.5\omega_p$, and the dielectric material is air ($\varepsilon_d = 1$). The other corresponding parameters of InSb are chosen as $m^* = 0.014 m_0$ (m_0 is the free electron mass in vacuum), $\omega_p = 12.6\text{THz}$, and $\varepsilon_\infty = 15.68$ [4].

As shown in the dispersion equation, the nonreciprocal effect is immediately observed. We first discuss the case of $\beta > 0$. An interesting feature is that the dispersion curve consists of two propagation bands with a gap between them. The lower curve starts from the origin, rises just to the right of the light line (the line marked as $\alpha_0 = 0$), bends over, and terminates when it reaches the dispersion curve of the bulk magneto plasmons (the line marked as $\alpha = 0$). The higher branch starts from the line of $\varepsilon_{xx} = 0$, and approaches the asymptotic frequency for the non-retarded magneto plasmons defined by $\varepsilon_d + \varepsilon_{xx} - i\varepsilon_{xz} = 0$. The reduced wave vector at which the upper band starts is specified by the equation of

$$\zeta_s^2 \equiv \left(\frac{c\beta}{\omega_p}\right)^2 = \frac{1 + \Omega_c^2}{1 - (\varepsilon_d/\varepsilon_\infty)^2 (1 + \Omega_c^2)/\Omega_c^2}, \quad (11)$$

where $\Omega_c = \omega_c/\omega_p$. In order to let ζ_s to be positive and finite, it must be satisfied that $\varepsilon_\infty/\varepsilon_d > \omega_H/\omega_c$, where $\omega_H = \sqrt{\omega_p^2 + \omega_c^2}$ is the hybrid cyclotron-plasmon frequency. For InSb and air, this is given by $\Omega_c \geq 0.064$. Therefore, the magnetic field should be at least 0.0643 Tesla to observe the higher band.

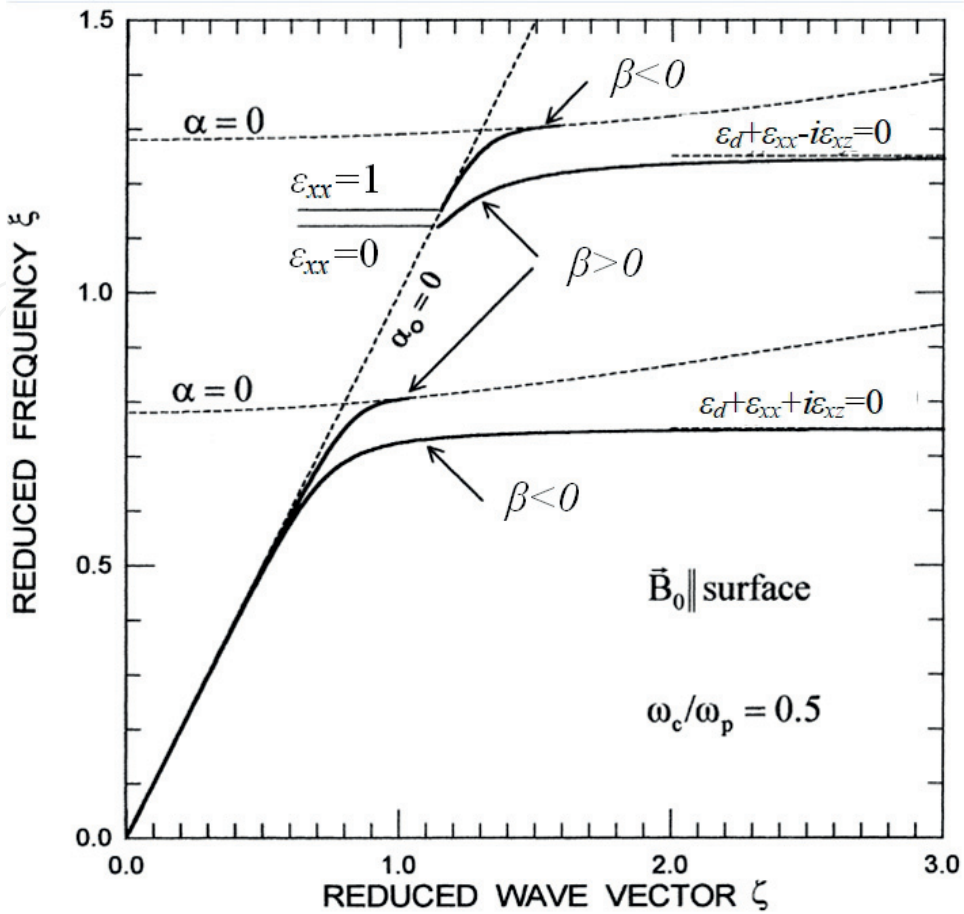


Figure 2. Dispersion curves of SMPs at the interface of InSb and air in the Voigt configuration (solid lines). $\omega_c = 0.5\omega_p$, $\xi = \omega/\omega_p$ and $\zeta = \beta c/\omega_p$ are normalized frequency and wave vector.

For $\beta < 0$, the lower band starting from the origin to the asymptotic value defined by $\varepsilon_d + \varepsilon_{xx} + i\varepsilon_{xz} = 0$. The higher band starts at the light line $\varepsilon_{xx} = 1$, rises to the right of the light line, and cutoff when it meets the higher bulk magneto plasmon curve $\alpha = 0$.

The two propagating band can be explained by **Figure 3**, where the Voigt dielectric constant is plotted as a function of the normalized angular frequency $\xi = \omega/\omega_p$. It can be seen that when $\omega_c = 0.5\omega_p$, there are two regions, where $\varepsilon_V < 0$. Because SMPs can only propagate on the surface of a material with negative permittivity, SMPs have two propagating bands on a plane surface.

2.2. Dispersion of SMPs in a symmetric slot waveguide

In order to expand the theory of SMPs in a subwavelength scale, we study the dispersion of SMPs in a slot waveguide with a lateral width in subwavelength scale. In this part, we study a symmetric structure, which is shown in **Figure 4**. An insulator layer (the permittivity is denoted by ε_d) with a width of w is sandwiched by two conductor layers. A TM-polarized electromagnetic wave (the magnetic field component is parallel to the y -axis) is propagating along the z -direction where $E_x(\mathbf{r}, \omega)$, $E_z(\mathbf{r}, \omega)$, $H_y(\mathbf{r}, \omega) \propto \exp[i(\beta z - \omega t)]$. An external static magnetic field B is applied uniformly along the y -axis, in a Voigt configuration. Therefore, according to the Maxwell equations, the electromagnetic field components in region I, II, and III can be written as

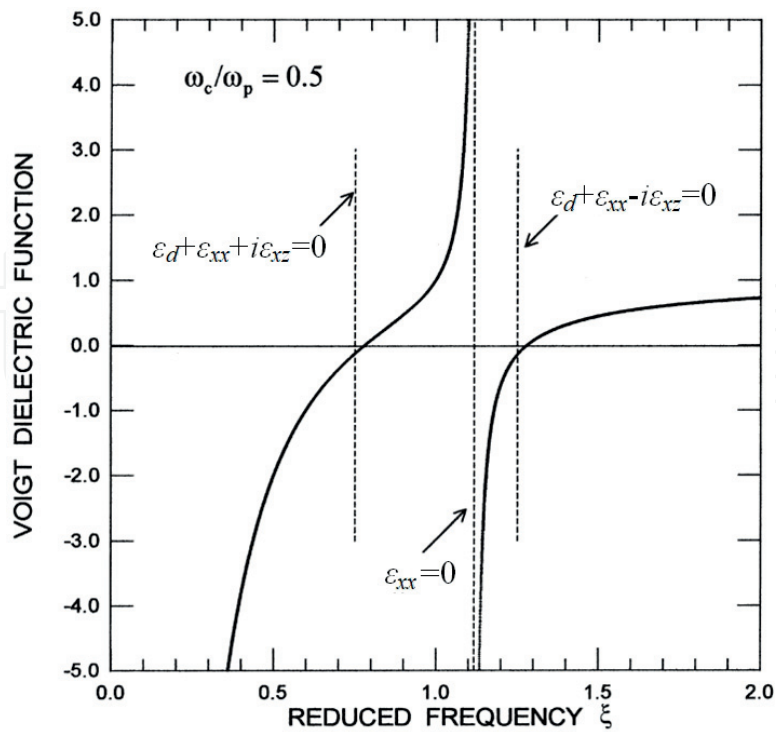


Figure 3. Voigt dielectric constant ϵ_V as a function of frequency.

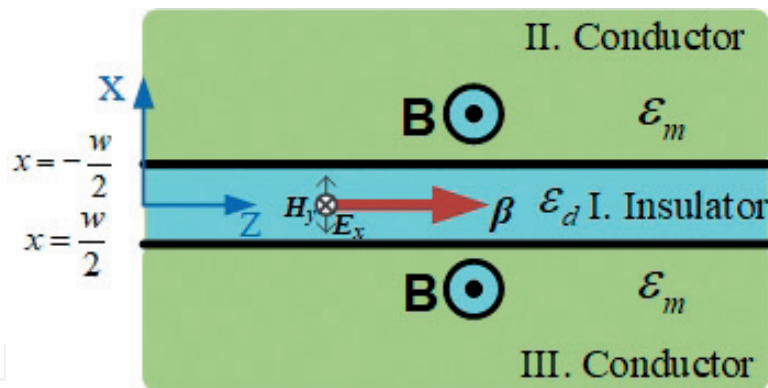


Figure 4. Schematic of SMPs propagating in a symmetric conductor-insulator-conductor structure in the Voigt configuration. The external static magnetic field B is applied along the y -axis.

$$H_y^{(I)} = Ae^{-\kappa_1 x} + Be^{\kappa_1 x} \quad (12)$$

$$E_z^{(I)} = -\frac{i\kappa_1}{\omega\epsilon_0\epsilon_d} (Ae^{-\kappa_1 x} - Be^{\kappa_1 x}) \quad (13)$$

$$H_y^{(II)} = Ce^{-\kappa_2(x-w/2)} \quad (14)$$

$$E_z^{(II)} = \frac{1}{i\omega\epsilon_0(\epsilon_{xx}^2 + \epsilon_{xz}^2)} \left(i\beta\epsilon_{xz} Ce^{-\kappa_2(x-w/2)} + \epsilon_{xx}\kappa_2 Ce^{-\kappa_2(x-w/2)} \right) \quad (15)$$

$$H_y^{(III)} = D e^{\kappa_3(x+w/2)} \quad (16)$$

$$E_z^{(III)} = \frac{1}{i\omega\epsilon_0(\epsilon_{xx}^2 + \epsilon_{xz}^2)} \left(i\beta\epsilon_{xz} D e^{\kappa_3(x+w/2)} - \epsilon_{xx}\kappa_3 D e^{\kappa_3(x+w/2)} \right) \quad (17)$$

where A, B, C, and D are undetermined coefficients. κ_1 , κ_2 and κ_3 are expressed by

$$\kappa_1^2 = \beta^2 - k_0^2\epsilon_d \quad (18)$$

$$\kappa_2^2 = \kappa_3^2 = \beta^2 - k_0^2\epsilon_V \quad (19)$$

Employing the boundary conditions at the two interfaces ($x = -w/2$ and $x = w/2$) yields

$$\left\{ \begin{array}{cc} \left[\frac{(\beta\epsilon_{xz} - i\epsilon_{xx}\kappa_2)}{(\epsilon_{xx}^2 + \epsilon_{xz}^2)} + \frac{i\kappa_1}{\epsilon_d} \right] e^{-\kappa_1 w/2} & \left[\frac{(\beta\epsilon_{xz} - i\epsilon_{xx}\kappa_2)}{(\epsilon_{xx}^2 + \epsilon_{xz}^2)} - \frac{i\kappa_1}{\epsilon_d} \right] e^{\kappa_1 w/2} \\ \left[\frac{(\beta\epsilon_{xz} + i\epsilon_{xx}\kappa_2)}{(\epsilon_{xx}^2 + \epsilon_{xz}^2)} + \frac{i\kappa_1}{\epsilon_d} \right] e^{\kappa_1 w/2} & \left[\frac{(\beta\epsilon_{xz} + i\epsilon_{xx}\kappa_2)}{(\epsilon_{xx}^2 + \epsilon_{xz}^2)} - \frac{i\kappa_1}{\epsilon_d} \right] e^{-\kappa_1 w/2} \end{array} \right\} \begin{pmatrix} A \\ B \end{pmatrix} = 0 \quad (20)$$

The nontrivial solution of these linear equations requires the vanishing of the coefficients determinant, and then we can derive the following relation:

$$\tanh\left(w\sqrt{\beta^2 - \epsilon_d k_0^2}\right) \left[1 + \left(\frac{\epsilon_d}{\epsilon_V}\right)^2 \frac{\beta^2 - \epsilon_V k_0^2}{\beta^2 - \epsilon_d k_0^2} + \left(\frac{\epsilon_d}{\epsilon_V}\right)^2 \left(\frac{\epsilon_{xz}}{\epsilon_{xx}}\right)^2 \frac{\beta^2}{\beta^2 - \epsilon_d k_0^2} \right] + 2 \frac{\epsilon_d}{\epsilon_V} \frac{\sqrt{\beta^2 - \epsilon_V k_0^2}}{\sqrt{\beta^2 - \epsilon_d k_0^2}} = 0 \quad (21)$$

Eq. (21) is the dispersion relation of TM-polarized SMPs in the Voigt configurations for the symmetric slot structure. It should be noted that, when $B = 0$, Eq. (21) becomes the dispersion relations of SPs in a MIM structure [43]; when $w \rightarrow \infty$, it becomes Eq. (10).

An intriguing feature of Eq. (21) is that due to the symmetric structure, the nonreciprocal effect of Eq. (10) is eliminated because only β^2 can be found in the equation. The dispersion curve is shown in **Figure 5**. Without loss of generality, here we also assume the conductor material is n-doped InSb. The width of the dielectric is $w = 0.1 \times 2\pi c/\omega_p$. It is found that $\beta > 0$ and $\beta < 0$ SMP waves have same dispersion curve when the magnetic field is applied (blue lines). In addition, the two propagating bands are remained. The higher band can also be explained by the effect of the applied magnetic field on the Voigt dielectric constant ϵ_V in **Figure 3**.

Although the dispersion curve is reciprocal, the mode distribution is still nonreciprocal in this structure, which is shown in **Figure 6**. The normalized electric field intensities of the SMPs modes indicate that with the magnetic field, the mode distribution becomes asymmetric. For the SMPs mode in the lower band, most of the energy is confined on the lower surface of the dielectric layer, while the energy is mostly confined on the upper surface in the higher frequency band.

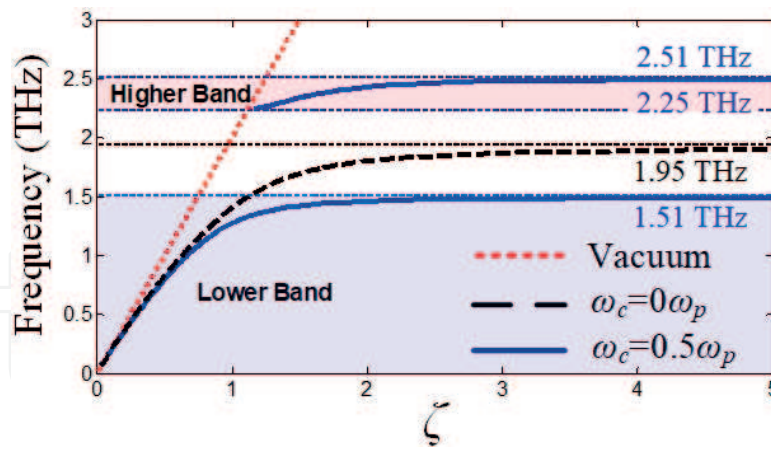


Figure 5. Dispersion curves of SMPs in a slot waveguide of InSb-air-InSb in the Voigt configuration (solid lines). $\omega = 0.1 \times 2\pi c/\omega_p$, $\zeta = \beta c/\omega_p$ is the normalized wave vector.

2.3. Dispersion of SMPs in an asymmetric slot waveguide

In this part, we study the dispersion of SMPs in an asymmetric slot waveguide with a lateral width in subwavelength scale, which is shown in **Figure 7**. The structure is similar with **Figure 4**,

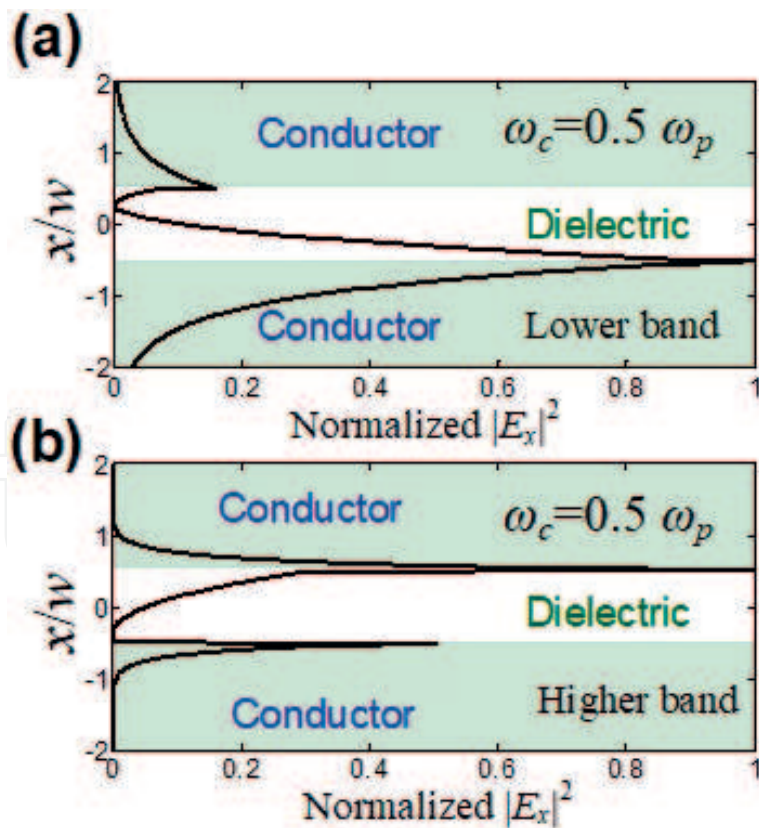


Figure 6. Normalized E_x intensities of SMPs mode along the x-axis under an external magnetic field of $\omega_c = 0.5 \omega_p$. (a) Lower band; (b) higher band.

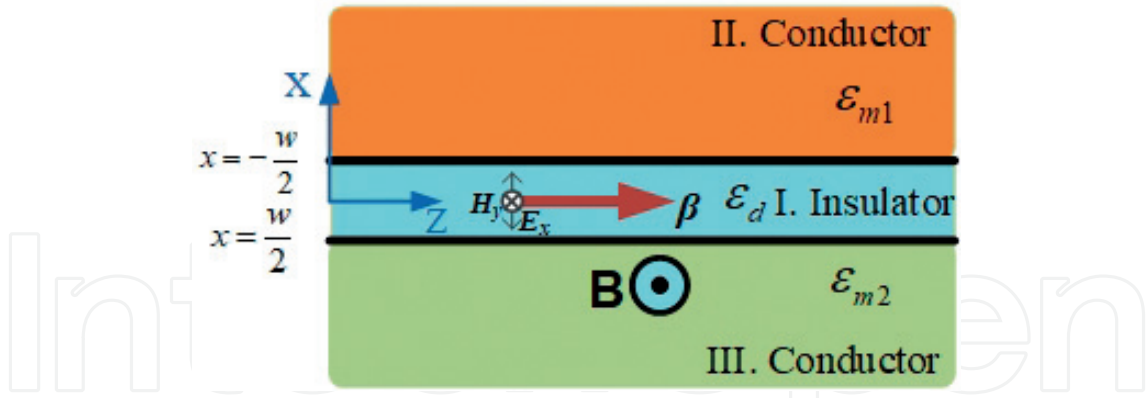


Figure 7. Schematic of SMPs propagating in an asymmetric conductor-insulator-conductor structure in the Voigt configuration. The external static magnetic field B is only applied on the conductor below the insulator.

an insulator layer is sandwiched by two conductor layers. However, the external magnetic field is only applied on one of the two conductor layers. In this geometry, the conductor of region III is anisotropic, and its permittivity is a tensor, as we discussed earlier, but the conductor of region II is isotropic. Therefore, according to the Maxwell equations, the electromagnetic field components in region I, II, and III can be written as

$$H_y^{(I)} = Ae^{-\kappa_1 x} + Be^{\kappa_1 x} \quad (22)$$

$$E_z^{(I)} = -\frac{i\kappa_1}{\omega\epsilon_0\epsilon_d}(Ae^{-\kappa_1 x} - Be^{\kappa_1 x}) \quad (23)$$

$$H_y^{(II)} = Ce^{-\kappa_2(x-w/2)} \quad (24)$$

$$E_z^{(II)} = -\frac{i\kappa_2}{\omega\epsilon_0\epsilon_m}Ce^{-\kappa_2(x-w/2)} \quad (25)$$

$$H_y^{(III)} = De^{\kappa_3(x+w/2)} \quad (26)$$

$$E_z^{(III)} = \frac{1}{i\omega\epsilon_0(\epsilon_{xx}^2 + \epsilon_{xz}^2)}\left(i\beta\epsilon_{xz}De^{\kappa_3(x+w/2)} - \epsilon_{xx}\kappa_3De^{\kappa_3(x+w/2)}\right) \quad (27)$$

where A , B , C , and D are undetermined coefficients. ϵ_m is the isotropic permittivity of region II. κ_1 , κ_2 and κ_3 are expressed by

$$\kappa_1^2 = \beta^2 - k_0^2\epsilon_d \quad (28)$$

$$\kappa_2^2 = \beta^2 - k_0^2\epsilon_m \quad (29)$$

$$\kappa_3^2 = \beta^2 - k_0^2\epsilon_V \quad (30)$$

Employing the boundary conditions at the two interfaces ($x = -w/2$ and $x = w/2$), it can be derived

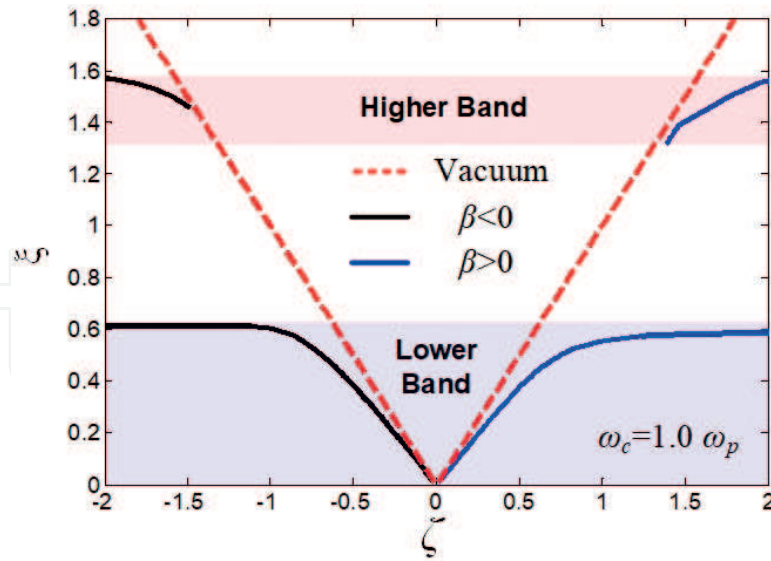


Figure 8. Dispersion curves of SMPs in an asymmetric slot waveguide in the Voigt configuration (solid lines). $w = 0.1 \times 2\pi c/\omega_p$, $\xi = \omega/\omega_p$ and $\zeta = \beta c/\omega_p$ are normalized frequency and wave vector, respectively.

$$\left\{ \begin{array}{cc} \left[\frac{i\kappa_2}{\varepsilon_m} - \frac{i\kappa_1}{\varepsilon_d} \right] e^{i\kappa_1 w/2} & \left[\frac{i\kappa_2}{\varepsilon_m} + \frac{i\kappa_1}{\varepsilon_d} \right] e^{-i\kappa_1 w/2} \\ \left[\frac{(i\beta\varepsilon_{xz} - \varepsilon_{xx}\kappa_3)}{i(\varepsilon_{xx}^2 + \varepsilon_{xz}^2)} + \frac{i\kappa_1}{\varepsilon_d} \right] e^{-i\kappa_1 w/2} & \left[\frac{(i\beta\varepsilon_{xz} - \varepsilon_{xx}\kappa_3)}{i(\varepsilon_{xx}^2 + \varepsilon_{xz}^2)} - \frac{i\kappa_1}{\varepsilon_d} \right] e^{i\kappa_1 w/2} \end{array} \right\} \begin{pmatrix} A \\ B \end{pmatrix} = 0 \quad (31)$$

Then we can derive the dispersion equation of SMPs in an asymmetric slot waveguide by the nontrivial solution of these linear equations:

$$\left\{ \frac{\sqrt{\beta^2 - k_0^2 \varepsilon_m} \sqrt{\beta^2 - k_0^2 \varepsilon_V}}{\beta^2 - \varepsilon_d k_0^2} \frac{1}{\varepsilon_m \varepsilon_V} + \frac{1}{\varepsilon_d^2} - i \frac{\beta \sqrt{\beta^2 - k_0^2 \varepsilon_m}}{\beta^2 - \varepsilon_d k_0^2} \frac{\varepsilon_{xz}}{\varepsilon_m \varepsilon_V \varepsilon_{xx}} \right\} \tanh \left(\sqrt{\beta^2 - \varepsilon_d k_0^2} w \right) + \left[\frac{\sqrt{\beta^2 - k_0^2 \varepsilon_V}}{\sqrt{\beta^2 - \varepsilon_d k_0^2}} \frac{1}{\varepsilon_d \varepsilon_V} + \frac{\sqrt{\beta^2 - k_0^2 \varepsilon_m}}{\sqrt{\beta^2 - \varepsilon_d k_0^2}} \frac{1}{\varepsilon_m \varepsilon_d} - i \frac{\beta}{\sqrt{\beta^2 - \varepsilon_d k_0^2}} \frac{\varepsilon_{xz}}{\varepsilon_d \varepsilon_V \varepsilon_{xx}} \right] = 0 \quad (32)$$

One can know by a glance from Eq. (32) that in an asymmetric slot waveguide, SMPs have nonreciprocal dispersion as those on a plane surface. In **Figure 8**, the dispersion curves of both $\beta > 0$ and $\beta < 0$ are plotted, when $w = 0.1 \times 2\pi c/\omega_p$, $\omega_c = 0.1\omega_p$. It can be seen that due to nonreciprocal effect, forward propagating and backward propagating SMPs have different cutoff frequencies.

3. Applications of slot SMPs

In recent years, several kinds of SMP devices that can manipulate electromagnetic fields in subwavelength scale have been proposed [46–49, 52–56]. However, most of them are focused

on the magnetic-field tunable property. The nonreciprocal effect and the two propagating bands are rarely utilized. In this section, we give three applications using the nonreciprocal effect, two propagating bands and magnetic field tuning properties, respectively. The SMPs applications are realized by semiconductors in the terahertz regime. However, the design principle can be used in any SMP devices.

3.1. Broadly tunable one-way terahertz plasmonic waveguides based on nonreciprocal effect of slot SMPs

With the rapid development in Terahertz (THz) technology in recent years, THz plasmonic components, e.g. waveguides, have been proposed due to the sub-wavelength confinement for miniaturized devices. However, most plasmonic waveguides are two-way waveguides, i.e. light waves propagate in both the forward and the backward directions. One-way-propagating waveguides are highly desired in splitters, switches and isolators. One method to realize one-way plasmonic devices are based on interference of SPs [66]. This effect is strongly sensitive to geometric structure variations. Another approach is by the nonreciprocal effect of SMPs under an external magnetic field. The dispersions of the forward and backward propagating SMPs terminate at different cut-off frequencies, making it possible to realize an absolute one-way plasmonic waveguide.

In this section, we propose a simple THz one-way sub-wavelength plasmonic waveguide that needs only 1 Tesla. By tuning the applied MF, the central frequency of the one-way-propagating frequency band is shifted from 1.5 to 0.36 THz when the MF is increased from 0.5 to 5 Tesla.

The schematic structure of the proposed waveguide is depicted in **Figure 9(a)**. It is composed of a metal-dielectric-semiconductor. The metal and the semiconductor layers are half-infinite and the thickness of the dielectric layer is w . The external static magnetic field is applied uniformly on the whole structure along the y -axis (as indicated by B), forming a Voigt configuration. Without loss of generality, we assume the metal, dielectric and semiconductor are Au, air and InSb, respectively. Although Au is a conductor, it resembles perfect conductors in the THz regime [67]. Therefore, it can be considered as an isotropic material even though the magnetic field is applied. In this approximation, the conclusion of Section 2.3 can be applied. **Figure 9(b)** shows the dispersion

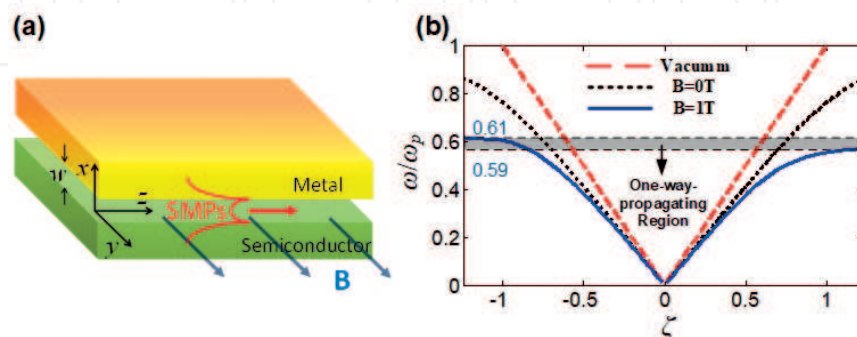


Figure 9. (a) Schematic structure of the one-way THz plasmonic waveguide. It is composed of metal (upper), dielectric (middle), and semiconductor (lower) layers. (b) Dispersion relations of the THz SMPs without and with an external magnetic field.

curves of the lower band of SMPs waves with ($B = 1$ Tesla) and without the external magnetic fields. It can be found that the dispersion curves are symmetric without the magnetic field. While, when magnetic field is applied, the dispersion curves of the two propagating waves become different. The cutoff frequency of the forward-propagating mode is $\omega/\omega_p = 0.59$, while that of the backward propagating mode is $\omega/\omega_p = 0.61$. This means that the THz waves in the frequency region of $\omega/\omega_p = [0.59, 0.61]$ (corresponding to $f = [1.18, 1.23]$ THz) can only propagate backwards.

Then simulations are then conducted by the finite element method (FEM) using COMSOL Multiphysics to verify the one-way effect. The results are plotted in **Figure 2 (a)-(d)**. When the magnetic field is not applied, the field distributions of the forward and backward propagating waves are the same (see (a) and (b), respectively). However, when there is 1 Tesla magnetic field, the forward-propagating THz wave is blocked (see **Figure 2(c)**), while the backward-propagating wave can still propagate through the slit (see **Figure 2(d)**) (there is no bright-dark field distribution in the slit as that in **Figure 2(a)** and (c) also confirms that no reflected SMP wave can be realized in the slit to interfere with the incident wave). The compared transmitted intensities of the forward and the backward propagating waves of Figure (c) and (d) are depicted in **Figure 2(e)**. It can be seen the one way region located at $\omega = [0.592, 0.612]\omega_p$, which agrees very well with the theoretical results.

The tuning ability of the one-way frequency band is also studied. By applying the non-retardation limit [22], i.e. substitute $\beta \gg k_0$ into Eq. (32), we have $\kappa_1 \approx \kappa_2 \approx \kappa_3 \approx \beta$, and $\beta w \gg 1$. Thus the cutoff frequencies of the forward and the backward propagating modes ω_{vf} and ω_{vb} can be calculated as

$$\omega_{vf} = \frac{1}{2} \left[\sqrt{\omega_c^2 + 4\omega_{ps}^2 \varepsilon_\infty / (\varepsilon_d + \varepsilon_\infty)} - \omega_c \right] \quad (33)$$

$$\omega_{vb} = \frac{1}{2} \left[\sqrt{\omega_c^2 + 4\omega_{ps}^2} - \omega_c \right] \quad (34)$$

Therefore both ω_{vf} and ω_{vb} are functions of ω_c , which indicate the one-way region can be tuned by the external magnetic field. The one-way bandwidth is obtained analytically as $\Delta\omega = \omega_{vf} - \omega_{vb}$, which increases with ε_d . According to Eq. (32), we calculate ω_{vf} and ω_{vb} versus B , and the permittivity of the dielectric layer, shown in **Figure 11(a)** and **(b)**, respectively. It is found that the magnetic field affects both the cutoff frequencies of the forward and backward propagating modes. However, the bandwidth of the one-way band $\Delta\omega$ depends little on B , but determined by the permittivity of the dielectric layer ε_d . This effect is owing to the asymmetry of the mode distribution caused by the magnetic field.

Based on this one-way waveguide structure, we also proposed a THz plasmonic switch. It should be noted that if we change the propagation direction of the applied magnetic field, the dielectric tensor matrix in Eq. (1) is transposed. As a result, the one-way-propagating band will not block the forward wave, but the backward wave. According to this principle, a T-shape waveguide is designed, as shown in **Figure 12**. The width of the waveguide, the magnetic field intensity, and the incident frequency are the same as those in **Figure 10(c)** and **(d)**. It is clearly seen that when the direction of the external MF is changed, a tunable THz plasmonic switch can be realized.

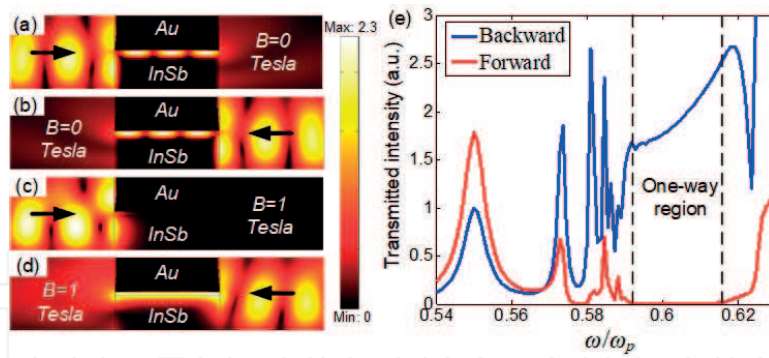


Figure 10. (a)-(d) FEM-simulated $|H_y|^2$ distribution of the forward and backward propagating waves in a sub-wave-length slit. The width and length of the slit are $0.1 \times 2\pi c/\omega_p$ and $300 \mu\text{m}$, respectively. The incident frequency is $\omega = 0.6\omega_p$, which is in the one-way frequency band. (e) Transmitted intensities of the forward (corresponding to (c)) and backward propagating (corresponding to (d)) waves when 1 Tesla magnetic field is applied.

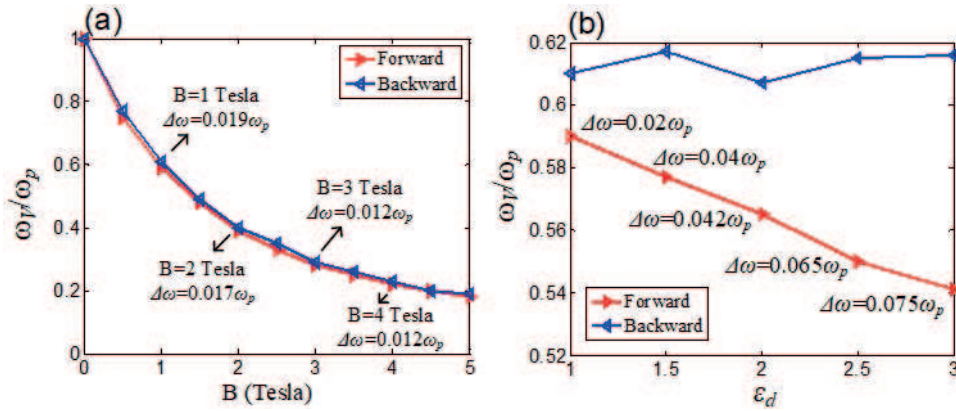


Figure 11. Effects of the applied magnetic field B (a) and the permittivity of the dielectric layer (b) on the one-way frequency band. ω_V represents the cutoff frequency. $\Delta\omega$ is the bandwidth of the one-way band.

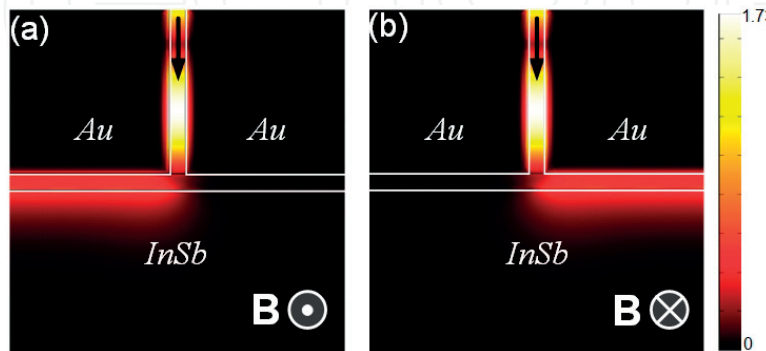


Figure 12. Field distributions of a designed THz plasmonic switch tuned by an external magnetic field. (a) the magnetic field is along $+y$ -axis. (b) the magnetic field is along $-y$ -axis.

3.2. A terahertz slow-light system with tunable group velocities in a broad frequency range by SMPs

In this part, we will apply the two bands of SMPs to a THz slow light system. Slow-light technology has great application potentials in telecommunications, data processing, and light-matter interactions. Compared with traditional electronic approaches [68], plasmonic approaches are easy to achieve because its subwavelength confinement of electromagnetic (EM) fields [69]. However, most slow light systems are not tunable so far, especially in the THz frequency region. In this section, we propose a tunable THz slow-light system based on SMPs with a semiconductor-insulator-semiconductor (SIS) structure. In this structure, both the frequency and the group velocity of the slowed-down THz wave can be tuned. More importantly, due to the existence of two SMPs bands, especially the higher band which has a wider tunable bandwidth, the proposed system has a very broad tunable bandwidth.

Because a plasmonic slow-light system is expected to have the same slow-light effect in both forward- and backward-propagating directions, we use a symmetric structure as shown in **Figure 13(a)** in which the nonreciprocal effect is eliminated. By the dispersion equation of Eq. (21), the dispersion curves of the SMPs in the structure when the external magnetic field is applied with intensities of 0, 0.5, 1 and 2 Tesla are plotted in **Figure 13(b)**. The width of the waveguide is $w = 0.1 \times 2\pi c/\omega_p = 15 \mu\text{m}$ ($\sim 1/20\lambda$ of 1 THz wave). It can be seen from the figure that with the increase of the magnitude of the external magnetic field, the two bands move toward opposite directions (as indicated by the blue arrow). In addition, the shift of the higher band dispersion curve is more obvious than the lower band dispersion curve. When the magnetic field increases from 0 to 2 T, the cutoff frequency of the lower band changes from 1.9 to 0.8 THz, while that of the higher band changes from 1.9 to 4.8 THz.

We then study the slowed-down characteristics of the structure. Since the analytical expression of the group velocity defined as $v_g = d\omega/d\beta$ cannot be obtained from Eq. (21), we calculate v_g numerically by fitting the dispersion curves in **Figure 13**. In **Figure 14(a)**, the normalized group velocity v_g with respect to c as a function of the incident frequency is plotted when the external magnetic fields are 0, 0.5, 1, and 2 Tesla. It shows that v_g can achieve $\sim 10^{-6}c$ in the structure for both the lower and higher modes in the lossless case. When the magnetic field is

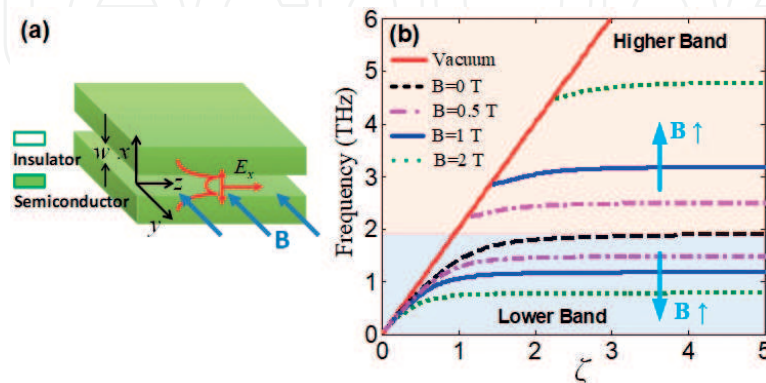


Figure 13. (a) Schematic structure of the THz plasmonic slow-light system. (b) Dispersion relations of the SMPs without and with an external magnetic field.

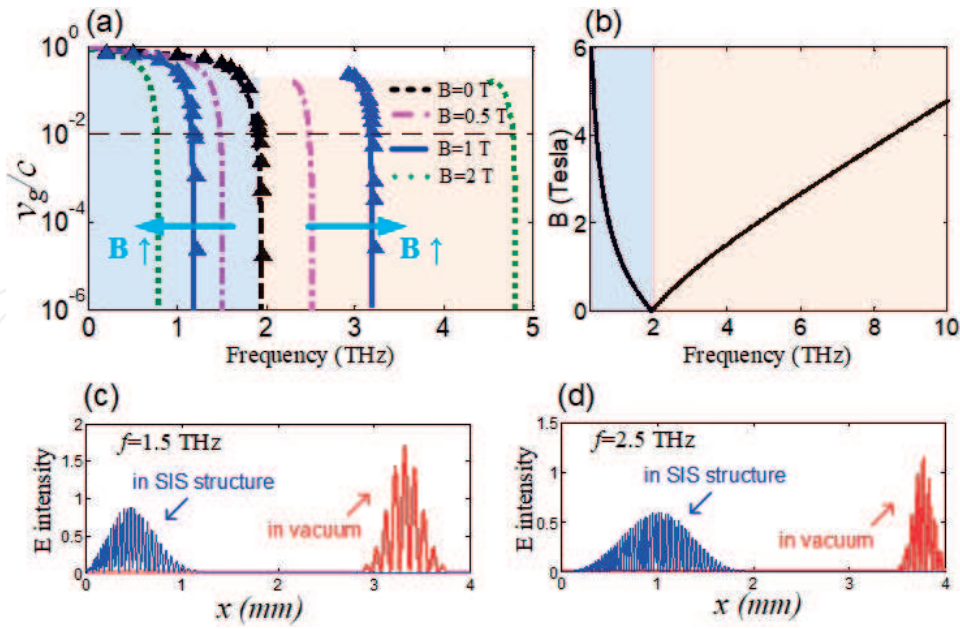


Figure 14. Slow-light effect of the structure tuned by an external magnetic field. The lower and the higher bands under the magnetic field are indicated by the blue and the pink shadows, respectively. (a) Normalized group velocity of the structure with 0 to 2 Tesla external magnetic fields (lines: Numerical results by fitting dispersion curves in **Figure 13(b)**; triangular points: FDTD simulation results). (b) Incident frequencies versus their corresponding needed magnetic fields. (c) and (d) FDTD simulations of THz pulses propagating in the slow-light waveguide compared with that propagating in vacuum after 15 ps for $f = 1.5$ THz and $f = 2.5$ THz, respectively, when a 0.5 Tesla magnetic field is applied. The pulse is launched at $x = 0$. Both the lower and higher band can slow down the THz waves.

increased from 0 to 2 Tesla, the corresponding frequency for $v_g < 10^{-6}c$ moves from 1.9 to 0.8 THz for the lower band, while that of the higher band moves from 1.9 to 4.8 THz. To verify these results, finite-difference time-domain (FDTD) simulations are conducted for $B = 0$ and 1 Tesla, respectively (shown as the triangular points). The group velocities of the simulation results agree well with the analytical results from Eq. (21). This verifies the slow-light effects of the system. More obvious FDTD simulated results of a slowed THz pulse in the structure are shown in **Figure 14(c)** and **(d)**. The incident frequencies are chosen as $f = 1.5$ THz and $f = 2.5$ THz, which are the frequencies corresponding to $v_g/c = 10^{-2}$ of the lower band and the higher band when a 0.5 Tesla magnetic field is applied, respectively. In the simulations, the THz pulses propagating in the slow-light system and in vacuum along the x -axis are compared. It shows that, for $f = 1.5$ THz, the THz pulse moves 3.3 mm in vacuum while only 0.4 mm in the structure after 15 ps. For $f = 2.5$ THz, the THz pulse moves 3.8 mm in vacuum while 1 mm in the structure after 15 ps. The reason on the larger simulated group velocity compared with the calculated one is that we added losses to InSb material in order to keep the simulation more stable, which may dramatically limit the achievable slow down factors and introduce losses [70]. Furthermore, the pulse is broadened because of the high dispersion of the system in the frequency region where the signal group velocity is low (the dispersion is proportional to $dv_g/d\omega$), which could be solved by using solitons in Kerr dielectrics [71].

Although direct relation of the magnetic field intensity B and the incident angular frequency ω is difficult to obtain, it is found that the slow light region is always close to the cut-off frequency of the SMPs modes, which can be derived analytically. From the non-retarded limit

of Eq. (21), the cutoff frequencies of the lower and the higher modes can be obtained by $1 + \epsilon_{xx} + i\epsilon_{xz} = 0$ and $1 + \epsilon_{xx} - i\epsilon_{xz} = 0$, respectively. Then we have

$$B = \pm \frac{m^*}{e} \left[\frac{\omega_p^2 \epsilon_\infty}{\omega(\epsilon_d + \epsilon_\infty)} - \omega \right] \quad (35)$$

where '+' represents $\omega < \omega_{sp}$, '-' denotes $\omega > \omega_{sp}$. $\omega_{sp} = \text{sqrt}[\omega_p^2/(1 + \epsilon_d)]$ is the surface plasma frequency. From Eq. (35), one can calculate the magnetic field needed to slow down the THz waves. In **Figure 14(b)**, the calculated magnetic fields versus the frequencies of the incident THz waves are depicted. It is found that when the magnetic field increases to 6 Tesla, the group velocities of waves in the region of [0.3, 10] THz can all be decreased. Therefore, a plasmonic slow-light system with broad band tuning range is achieved.

From the results in **Figure 14(a)**, it is inferred that the group velocity can also be tuned by changing the intensity of the magnetic field. We choose 1 and 3 THz in the lower and higher bands, respectively. We then calculate their corresponding group velocities dependent on B , which are shown in **Figure 15(a)** and **(b)**, respectively. When the magnetic field is increased, the frequency- v_g curves corresponding to the lower band and higher bands moves to the

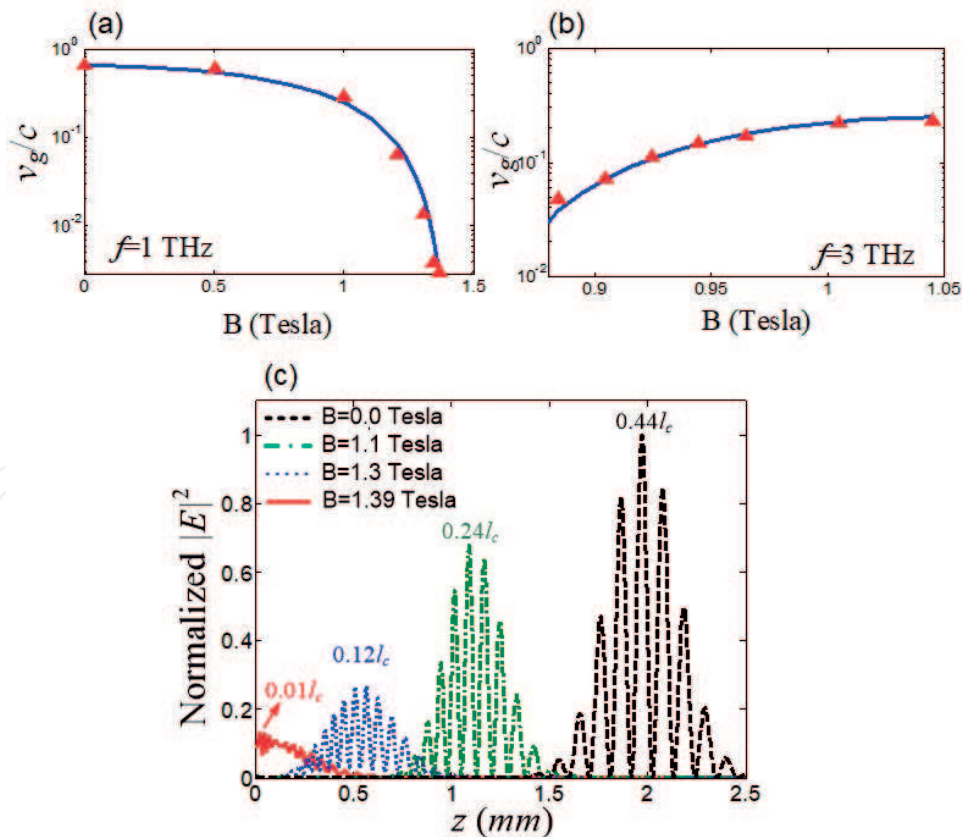


Figure 15. Group velocity of a monochromatic wave tuning by the magnetic field. (a) and (b) $f = 1$ THz (in the lower band) and $f = 3$ THz (in the higher band), respectively. Blue lines: Results from the analytical model. Red dots: FDTD simulation results. (c) FDTD simulations of THz pulses propagating in the slow-light waveguide. The frequency of the incident wave is 1 THz. When the magnetic fields are 0, 1.1, 1.3, and 1.4 Tesla, the peak of the pulse moves $0.01l_c$, $0.12l_c$, $0.24l_c$, and $0.44l_c$ after the THz pulse is launched 15 ps , respectively, where l_c is defined as $l_c = 15 \text{ ps} \times c$.

opposite directions. Therefore, v_g in the lower band decreases with the magnetic field, while v_g in the higher band increases. When the magnetic field increases from 0 to 1.36 Tesla, the group velocity of 1 THz frequency decreases from $0.65c$ to $10^{-3}c$. For frequency at 3 THz, the required magnetic field is from 1.04 to 0.88 Tesla in order to slow down the wave from $0.23c$ to $0.048c$. In **Figure 15(c)**, the FDTD simulated magnetic-field-tunable group velocity of a THz pulse is depicted. The incident frequency is 1 THz. It can be found that when B is increased, the distance Terahertz pulse moves become shorter and shorter. When $B = 1.39$ Tesla, it can be found that the THz pulse moves only $0.01l_c$ after it is launched 15 ps, where l_c is the corresponding moving distance of light in vacuum. It is worth noting that the loss also increases with the magnetic field. Therefore, in addition to the broad tuning range, the group velocity can also be flexibly tuned in the proposed slow-light system.

We then discuss the effects of the material loss on the tuning properties of the slow-light system. It is reported that the slowdown factor may be limited by the material losses [70]. This phenomenon is also observed with this structure. In a semiconductor, the loss is mainly caused by the collision of charge carriers, characterized by the collision frequency ν in Eqs. (2)–(4). For a small loss, we have $\nu = 0.01\omega_p$, the group velocity v_g is in the order of $10^{-2} \sim 10^{-1}c$. It is increased with the loss, which can be found in **Figure 16**. In addition, owing to the loss, the group velocity no longer decreases monotonously with the frequency, but increases dramatically at a resonant frequency after reaching the minimum value. Therefore, the tuning mechanism of the proposed structure is still valid in a lossy system. The tunable range restricted by the material loss could be effectively compensated by using active materials [71], designing doping levels, etc.

3.3. Terahertz plasmonic slit lenses with tunable focal length

Among various plasmonic devices, planar plasmonic slit lenses (PSLs) are often used to realize integrated optical collimators [72–74]. Plasmonic slit lenses consist of a metallic slab with several nanoslits with various widths, thicknesses and material compositions. When light wave propagates through these slits, it has different phase retardations. By adjusting the materials and geometric parameters of the slits, phase control is able to be realized. Compared

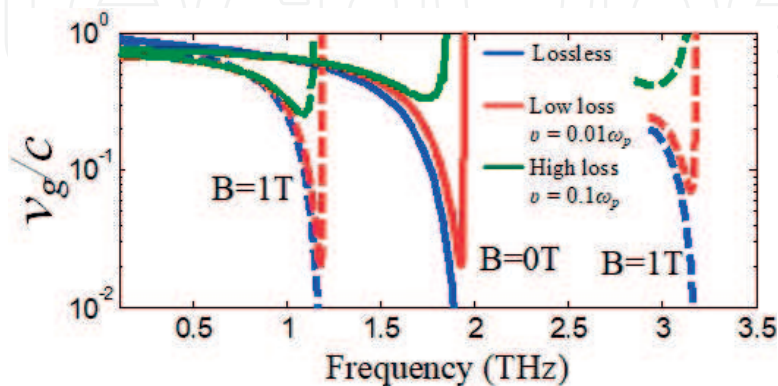


Figure 16. Effects of loss on the tuning properties of the slow-light system. The loss is characterized by the collision frequency ν of free carriers.

to other lenses, PSLs have relatively simple structures. In this part, using the magnetic field tuning ability of SMPs, we present an active THz PSL. The focal length of the PSL can be actively tuned by an external magnetic field.

The PSL structure is shown in **Figure 17**. It is composed a symmetric 2D InSb slab surrounded by air, and perforated with $2N-1$ slits. The thickness of the slab is h ; the lens width is d ; and the width of the i -th slit is denoted by w_i . The incident plane wave is TM-polarized with frequency f . Therefore, each slit can be considered as an SIS waveguide structure with finite length in z -direction, or a single-mode Fabry-Perot (F-P) cavity, with the refractive index of n_1 above the slit, n_3 below the slit, and $n_{eff} = \beta/k_0$ the effective refractive index of the slit. β is the propagating constant of SMPs that can be calculated by Eq. (21). In consequence, according to Fresnel equations, the phase retardation $\Delta\varphi$ of the magnetic field component H_y through a slit is expressed as

$$\Delta\varphi = \arg \left[\frac{H_{y0}}{H_{yi}} \right] = \arg \left[\frac{t_{01}t_{12}e^{i\alpha}}{1 - r_{10}r_{12}e^{i2\alpha}} \right] \quad (36)$$

where H_{yi} and H_{y0} are the incident magnetic field at the entrance and transmitted magnetic field at the exit, respectively. $\alpha = k_0 \times h \times n_{eff}$, $r_{10} = (n_1 - n_{eff})/(n_1 + n_{eff})$, $r_{12} = (n_2 - n_{eff})/(n_2 + n_{eff})$, $t_{01} = 1 - r_{10}$, $t_{12} = 1 + r_{12}$. Therefore, according to Eq. (21), different slit widths and magnetic fields provide different propagation constants, and also the phases. In the following design procedures, without loss of generality, we set the thickness of the slab as $h = 300 \mu\text{m}$, and the incident frequency is $f = 1 \text{ THz}$, thus $\varepsilon_V = -45.6 + 16.4i$ for $B = 0 \text{ Tesla}$ and $\varepsilon_V = -14.3 + 6.6i$ for $B = 1 \text{ Tesla}$.

Since phase retardation is the key factor in the design, we study the impact of the external magnetic field on $\Delta\varphi$ first. The dispersion of SMPs in an InSb-air-InSb structure considering the loss of InSb is depicted in **Figure 18(a)**, according to Eq. (21). It is found from the figure

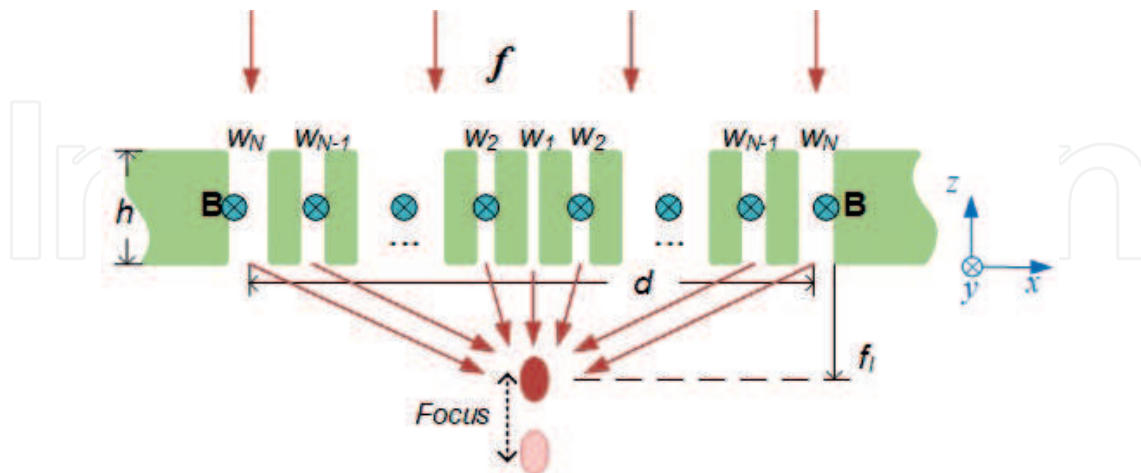


Figure 17. Schematic structure of the tunable THz PSL. The structure consists of an InSb slab tunable by an external magnetic field B , and perforated with $2N-1$ sub-wavelength slits. THz waves are indicated by the red arrows. They have different phase retardations after the slits, thus focusing can be realized by modulating those phases. The thickness of the slab is denoted by h . the width of the i -th slit from the middle to the two sides is w_i . f_f denotes the focal length of the lens. The external magnetic field B is applied along the y -axis in order to change the focal length.

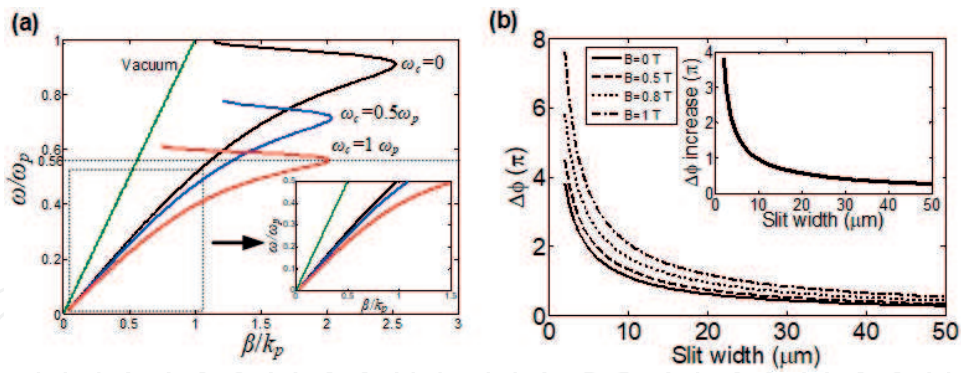


Figure 18. (a) Dispersion relation of SMPs in an InSb-air-InSb structure. The electronic dissipation is considered. Electromagnetic wave in vacuum and magnetoplasmons (MPs) under the magnetic field of $\omega_c = 0$, $\omega_c = 0.5\omega_p$, and $\omega_c = 1\omega_p$ are denoted by the green, black, blue and red lines, respectively. The inset shows the enlarged view of the low-frequency region. The insulator width is set as $w = 0.1 \times 2\pi c/\omega_p$. (b) Phase retardation of a single slit under external magnetic field of different intensity. The incident frequency is 1THz, and the thickness of the slab is $300 \mu\text{m}$. The inset shows the corresponding increase of $\Delta\varphi$ against the slit width for a magnetic field from 0 Tesla to 1 Tesla.

that, when the magnetic field is increased, the dispersion curve moves toward lower-frequencies. In other words, for a certain frequency, the propagation constant increases with the increase of the magnetic field, which can be seen clearly in the inset of **Figure 18(a)**. As a result, it can be inferred from Eq. (36) that the phase retardation of the propagation mode in a slit is increased with the increase of the magnetic field. The curves of $\Delta\varphi$ versus slit width under several magnetic field intensities are plotted in **Figure 18(b)**, calculated by Eq. (36). It shows that for a single slit, the phase retardation becomes larger when an external magnetic field is applied. The reason is that with the increase of the external magnetic field, the negative real part of bulk dielectric constant ε_V increases, which results in an increase of the effective refractive index of the slit. Therefore, the phase retardation is increased. It can also be found from **Figure 18(b)** that the change of the phase retardation of narrower slits is more obvious than that of wider slits under the same magnetic field.

Then following Eqs. (21) and (36), we design a lens with focal length of $f_l = 7\lambda$ for $B = 0$, the slit positions and widths are shown in **Figure 19(a)**. The total width of the lens and slit number are $d = 2 \text{ mm}$ and $2N-1 = 41$, respectively. Therefore, when an external magnetic field is applied, the phase curve at the slab output surface will be more convex (see **Figure 19(b)**) with the magnetic field. In analogous to a conventional lens, the focal length of the proposed lens will be reduced by the magnetic field.

To verify the tunability of the PSL, we calculate the distributions of magnetic field intensity of the electromagnetic field by FDTD simulations. The results are shown in **Figure 20**. The magnetic field intensity distributions of the lens for $B = 0 \text{ Tesla}$ and $B = 1 \text{ Tesla}$ are shown in **Figure 20(a)** and **(b)**, respectively. An obvious of focal length change is observed. From the dependence of the focal length on the intensity of applied magnetic field shown in **Figure 20(c)**, it is found that it is changed by 3λ (from 5.92λ to 2.87λ). There is also a deviation of the calculated focal length (5.92λ) from the designed one (7λ), and some strong side lobes appear. This focal shift effect is caused by both the small Fresnel number (about 1.6 for our structure) and SMPs interactions between the slits [74]. We then change the designed parameters such as

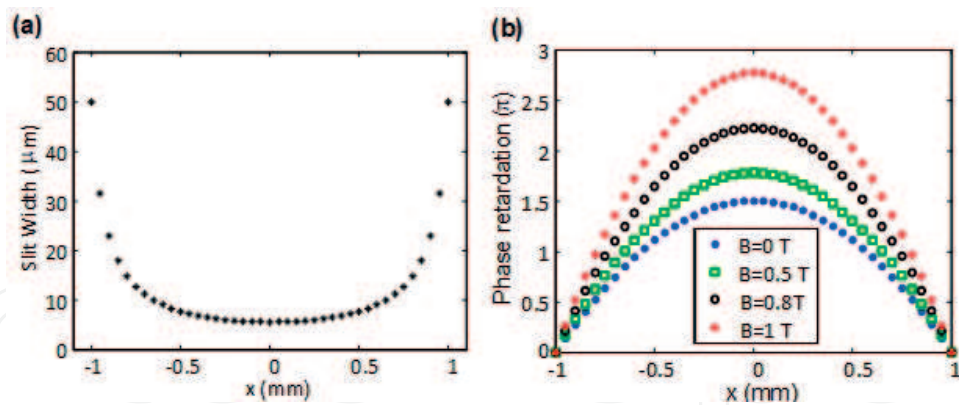


Figure 19. Design of a tunable THz plasmonic lens with focal length of 7λ and $d = 2$ mm, $N = 21$. (a) the slit position and corresponding slit width of the designed structure. (b) the relative phase retardation of the slits under magnetic fields of 0, 0.5, 0.8 and 1 Tesla.

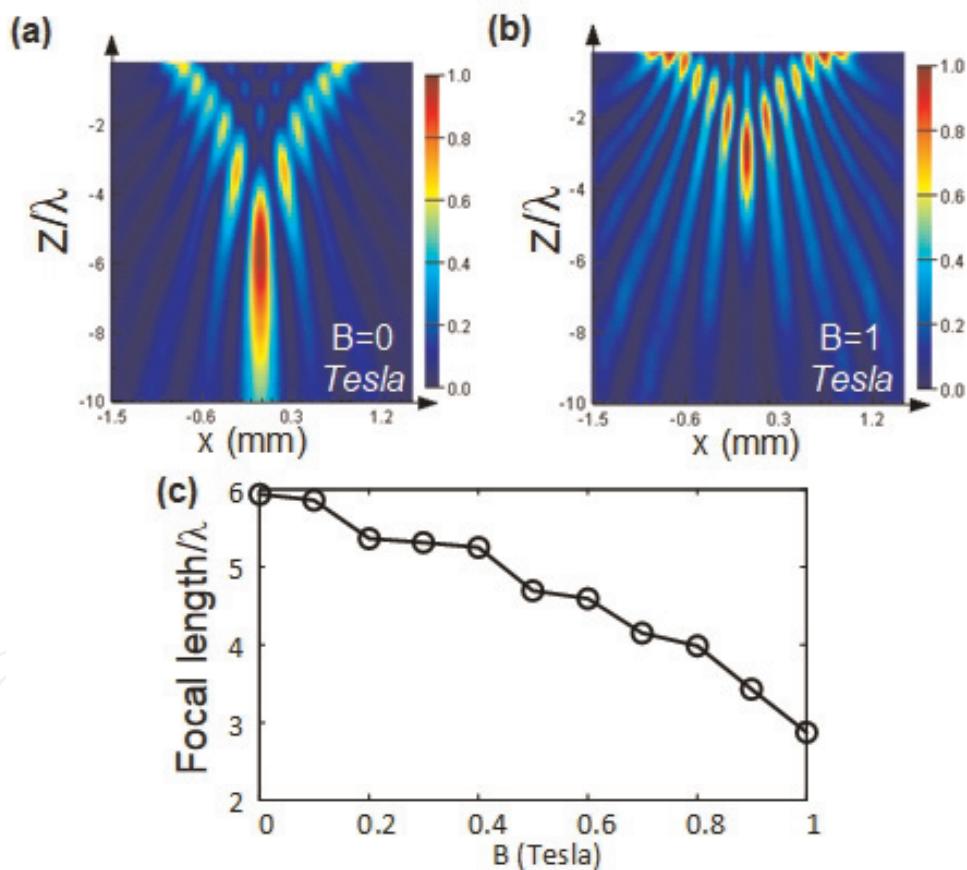


Figure 20. Magnetic field modulation on the THz PSL. (a), (b) $|H_y|^2$ distributions of the structure when the external magnetic field is 0 Tesla and 1 Tesla, respectively. (c) FDTD-calculated focal length when the external magnetic field is increased from 0 Tesla to 1 Tesla.

the lens width, the slit number, and designed focal length. The results are shown in **Figure 21**. It is found that, compared with slit number and designed focal length, the slit width d has a greater impact on the focal length change. The reason is that for a larger lens width, the

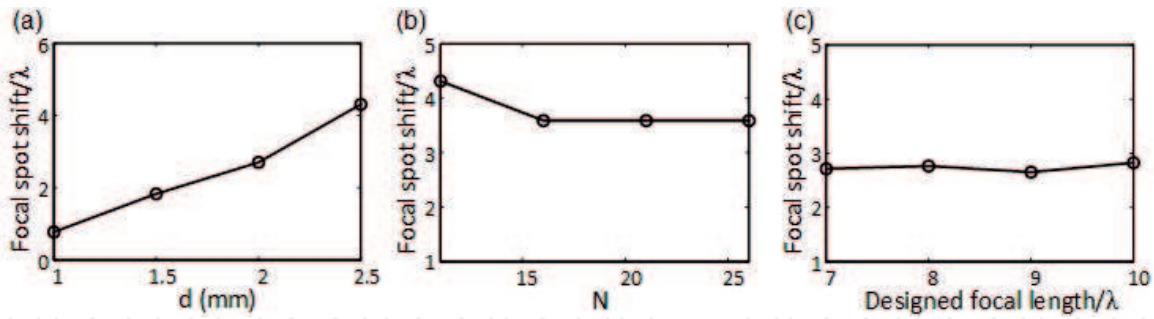


Figure 21. Focal length change caused by an external magnetic field increase from 0 to 1 Tesla as a function of various lens parameters. (a) Lens width changes as $d = 1$ mm, 1.5 mm, 2 mm, and 2.5 mm, when the designed focal length and slit number are fixed at $f_l = 10\lambda$, $2N-1 = 21$, respectively; (b) N changes as 11, 16, 21, and 26, when the designed focal length and lens width are fixed at $f_l = 10\lambda$, $d = 2.5$ mm; (c) designed focal lengths changes as 7λ , 8λ , 9λ , 10λ , and the length width and slit number are fixed as $d = 2$ mm, $2N-1 = 41$.

difference of the side slit width and middle slit width is greater. Therefore, the change of the phase curve on the exit plane of the slab is larger when an external magnetic field is applied.

We then investigate a lens with two monotonically increased sets of slits. The lens width and slit number are set as $d = 3$ mm and $N = 31$, as shown in **Figure 22(a)**. The designed focal length remains 7λ . The structure has two monotone intervals: $[0$ mm, 0.9 mm], and $[0.9$ mm, 1.5 mm]

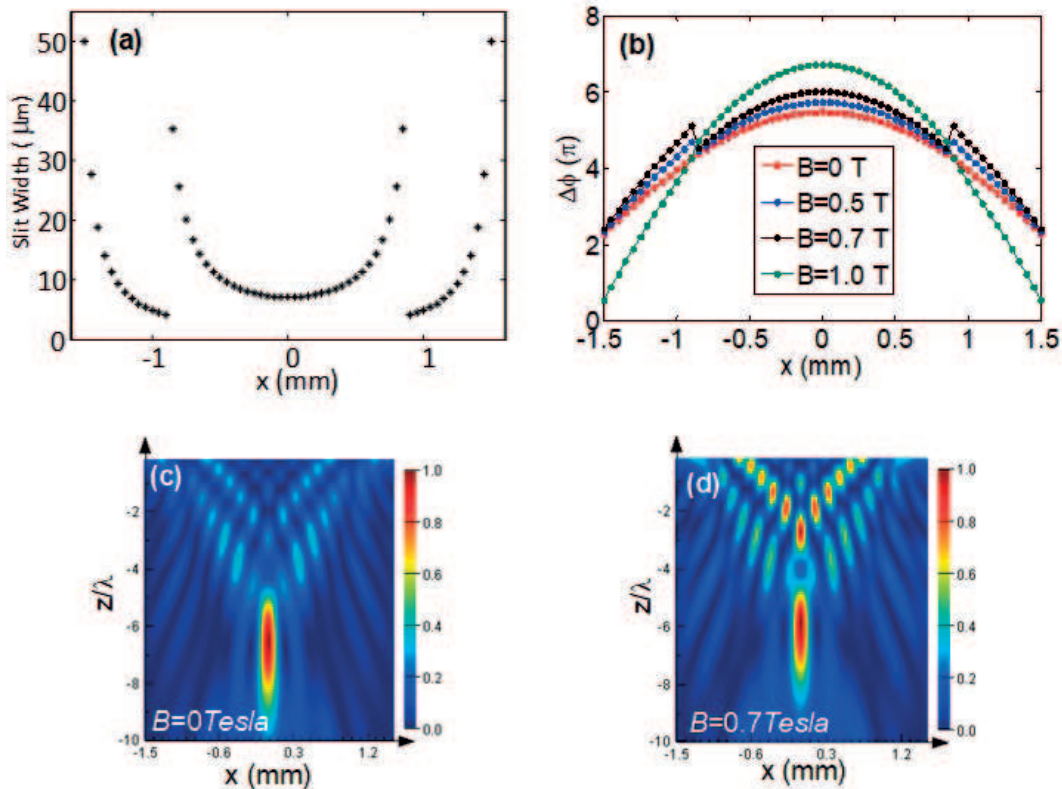


Figure 22. Bi-focus pattern by an external magnetic field. The parameters are same as the lens in **Figure 20**, except $d = 1$ mm, $N = 31$. (a) the slit position and corresponding slit width of the lens. (b) Phase retardation of the slits under different external magnetic fields. (c) and (d) $|H_y|^2$ distributions under a magnetic field of $B = 0$ and 0.7 Tesla, respectively.

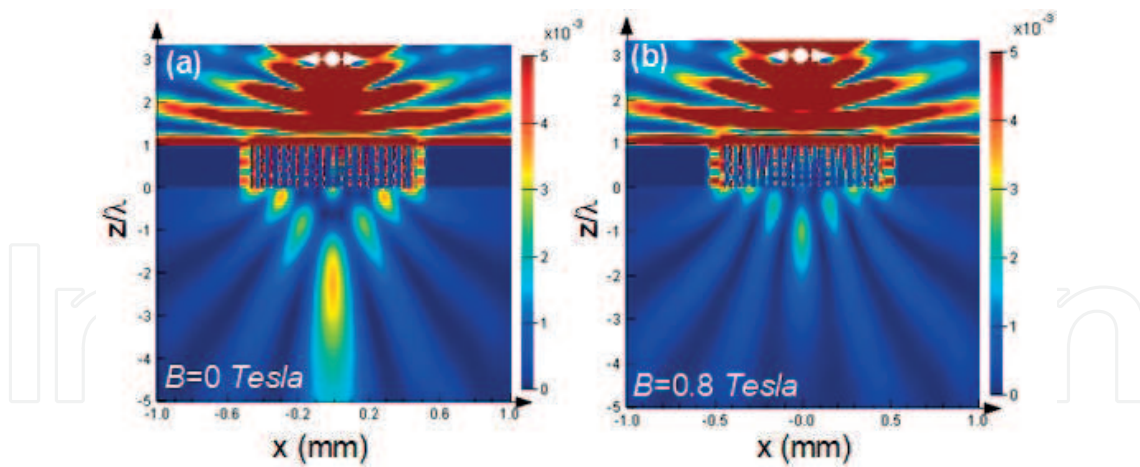


Figure 23. Magnetic-field tunable lens for a dipole source imaging. The designed object and image distances are both 3λ . The source is an electric dipole with the electric field vibration direction perpendicular to the z -axis, which is represented by a white circle on the top portion of the two figures. (a) $|H_y|^2$ distribution under a magnetic field of $B = 0$ Tesla. The obtained image distance is 2.25λ . (b) $|H_y|^2$ distribution under a magnetic field of $B = 0.8$ Tesla. The obtained image distance is 0.99λ .

from the middle to the two sides. The corresponding slit phase retardations are shown in **Figure 22(b)**. When the magnetic field increases, phase retardations of the two intervals grow asynchronously. Therefore, a discontinuous jump appears between the two intervals (see $B = 0$ and 0.7 Tesla for comparison). The field distribution of the transmitted wave at $B = 0$ Tesla and $B = 0.7$ Tesla (where the largest jump appears) are depicted in **Figure 22(c)** and **(d)**. It shows that when the magnetic field is 0.7 Tesla, we can achieve two focal spots along the z -axis.

Last but not least, a magnetic-field tunable lens for a dipole source imaging is proposed. The source is an electric dipole with the electric field vibration direction perpendicular to the z -axis. The designed object distance and image distance are both 3λ . The distributions of magnetic field intensity for the external magnetic field of $B = 0$ Tesla and $B = 0.8$ Tesla are depicted in **Figure 23(a)** and **(b)**, respectively. It shows that the obtained image distance is 2.25λ and 0.99λ for $B = 0$ and 0.8 Tesla, respectively.

4. Summary

In this chapter, we give a brief review on surface magneto plasmons. The theory of SMPs on a plane metal/conductor surface is reviewed. Our recent research on the theories of SMPs in symmetric and asymmetric slot waveguide is also presented. We also give the applications of SMPs based on their unique and intriguing properties, such as the nonreciprocal effect, two propagating bands, and tunability by an external magnetic field. A one-way THz waveguide, a THz broadly tunable slow-light system, and a focal length tunable plasmonic slit lens are presented, which show SMPs have big possibilities in applications of tunable plasmonic devices. Although the applications of SMPs have some drawbacks so far, including large loss and strong magnetic fields, with the rapid development of plasmonics, SMPs may open a new avenue of manipulating lights in subwavelength range.

Author details

Bin Hu

Address all correspondence to: hubin@bit.edu.cn

Beijing Engineering Research Center for Mixed Reality and Advanced Display, School of Optics and Photonics, Beijing Institute of Technology, Beijing, China

References

- [1] Barnes WL, Dereux A, Ebbesen TW. Surface plasmon subwavelength optics. *Nature*. 2003; **424**(6950):824-830
- [2] Raether H. In: Hohler G, editor. *Surface Plasmons on Smooth and Rough Surfaces and on Gratings*. Berlin: Springer; 1988
- [3] Palik ED, Furdyna JK. Infrared and microwave magnetoplasma effects in semiconductors. *Reports on Progress in Physics*. 1970; **33**(3):1193-1322
- [4] Brion JJ, Wallis RF, Hartstein A, Burstein E. Theory of surface magnetoplasmons in semiconductors. *Physical Review Letters*. 1972; **28**(22):1455-1458
- [5] Brion JJ, Wallis RF. Theory of pseudosurface polaritons in semiconductors in magnetic fields. *Physical Review B*. 1974; **10**(8):3140-3143
- [6] Wallis RF, Brion JJ, Burstein E. Theory of surface polaritons in anisotropic dielectric media with application to surface magnetoplasmons in semiconductors. *Physical Review B*. 1974; **9**(8):3424-3437
- [7] Kushwaha MS, Halevi P. Magnetoplasma modes in thin films in the faraday configuration. *Physical Review B*. 1987; **35**(8):3879-3889
- [8] Chiu KW, Quinn JJ. Magnetoplasma surface waves in metals. *Physical Review B*. 1972; **5**(12):4707-4709
- [9] De Wames RE, Hall WF. Magnetic field effect on plasma-wave dispersion in a dielectric layer. *Physical Review Letters*. 1972; **29**(3):172-175
- [10] Flahive PG, Quinn JJ. Surface waves of an electron-hole plasma in a uniform magnetic field. *Physical Review Letters*. 1973; **31**(9):586-589
- [11] Brion JJ, Wallis RF, Hartstein A, Burstein E. Interaction of surface magnetoplasmons and surface optical phonons in polar semiconductors. *Surface Science*. 1973; **34**(1):73-80
- [12] Hartstein A, Burstein E, Palik ED, Gammon RW, Hennis BW. Investigation of optic-phonon—Magnetoplasmon-type surface polaritons on n-InSb. *Physical Review B*. 1975; **12**(8):3186

- [13] Palik ED, Kaplan R, Gammon RW, Kaplan H, Wallis RF, Quinn JJ. Coupled surface magnetoplasmon-optic-phonon polariton modes on InSb. *Physical Review B*. 1976;**13**(6):2497
- [14] Eguiluz A, Quinn JJ. Magnetoplasma surface waves in solids with diffuse electron density profiles. *Physical Review B*. 1976;**13**(10):4299-4305
- [15] Yi KS, Quinn JJ. Magnetoplasma surface waves of a degenerate semiconductor in the Faraday geometry: Effect of the presence of a metallic screen. *Physical Review B*. 1980;**22**(12):6247-6253
- [16] Tyler IL, Fischer B, Bell RJ. On the observation of surface magnetoplasmons. *Optics Communications*. 1973;**8**(2):145-146
- [17] Kaplan H et al. Calculation of attenuated-total-reflection spectra of surface magnetoplasmons on semiconductors. *Journal of the Optical Society of America. A*. 1974;**64**(11):1551-1562
- [18] Fisher AD. Optical guided-wave interactions with magnetostatic waves at microwave frequencies. *Applied Physics Letters*. 1982;**41**(9):779
- [19] Remer L et al. Nonreciprocity in the optical reflection of magnetoplasmas. *Physical Review B*. 1984;**30**(6):3277
- [20] Stamps RL, Camley RE. Focusing of magnetoplasmon polaritons. *Physical Review B*. 1985;**31**:4924
- [21] Camley RE. Nonreciprocal surface waves. *Surface Science Reports*. 1987;**7**(3-4):103-187
- [22] Kushwaha M, Halevi P. Magnetoplasmons in thin films in the Voigt configuration. *Physical Review B*. 1987;**36**(11):5960-5967
- [23] Glass N. Nonreciprocal diffraction via grating coupling to surface magnetoplasmons. *Physical Review B*. 1990;**41**(11):7615
- [24] Boardman A, Shabat M, Wallis R. Nonlinear surface magnetoplasmon waves on a semiconductor. *Optics Communications*. 1991;**86**(5):416-422
- [25] Elmzoughi F, Tilley D. Surface and guided-wave polariton modes of magnetoplasma films in the Voigt geometry. *Journal of Physics: Condensed Matter*. 1994;**6**(23):4233
- [26] Safarov V et al. Magneto-optical effects enhanced by surface plasmons in metallic multilayer films. *Physical Review Letters*. 1994;**73**(26):3584-3587
- [27] Hermann C et al. Surface-enhanced magneto-optics in metallic multilayer films. *Physical Review B*. 2001;**64**:235422
- [28] Kushwaha MS. Plasmons and magnetoplasmons in semiconductor heterostructures. *Surface Science Reports*. 2001;**41**(1-8):1-416
- [29] Ebbesen T et al. Extraordinary optical transmission through sub-wavelength hole arrays. *Nature*. 1998;**391**(6668):667-669

- [30] Ozbay E. Plasmonics: Merging photonics and electronics at nanoscale dimensions. *Science* (New York, N.Y.). 2006;**311**(5758):189-193
- [31] Ritchie RH et al. Surface-plasmon resonance effect in grating diffraction. *Physical Review Letters*. 1968;**21**(22):1530-1533
- [32] Economou E. Surface plasmons in thin films. *Physical Review*. 1969;**182**(2):539-554
- [33] Marschall N, Fischer B, Queisser H. Dispersion of surface plasmons in InSp. *Physical Review Letters*. 1971;**27**(2):95-97
- [34] Knop K. Rigorous diffraction theory for transmission phase gratings with deep rectangular grooves. *Journal of the Optical Society of America*. 1978;**68**(9):1206
- [35] Moreland J, Adams A, Hansma PK. Efficiency of light emission from surface plasmons. *Physical Review B*. 1982;**25**(4):2297-2300
- [36] Sheng P, Stepleman R, Sanda P. Exact eigenfunctions for square-wave gratings: Application to diffraction and surface-plasmon calculations. *Physical Review B*. 1982;**26**(6):2907-2916
- [37] Weber M, Mills D. Interaction of electromagnetic waves with periodic gratings: Enhanced fields and the reflectivity. *Physical Review B*. 1983;**27**(5):2698-2709
- [38] Sambles J, Bradbery G, Yang F. Optical excitation of surface plasmons: An introduction. *Contemporary Physics*. 1991;**32**(3):173-183
- [39] Yang F, Sambles J, Bradberry G. Long-range surface modes supported by thin films. *Physical Review B*. 1991;**44**(11):5855-5872
- [40] Lochbihler H. Surface polaritons on gold-wire gratings. *Physical Review B*. 1994;**50**(7):4795-4801
- [41] Ebbesen TW, Genet C, Bozhevolnyi SI. Surface-plasmon circuitry. *Physics Today*. 2008;**61**(5):44-50
- [42] Dionne J et al. Plasmon slot waveguides: Towards chip-scale propagation with sub-wavelength-scale localization. *Physical Review B*. 2006;**73**:035407
- [43] Kurokawa Y, Miyazaki H. Metal-insulator-metal plasmon nanocavities: Analysis of optical properties. *Physical Review B*. 2007;**75**:035411
- [44] Belotelov V, Doskolovich L, Zvezdin A. Extraordinary magneto-optical effects and transmission through metal-dielectric plasmonic systems. *Physical Review Letters*. 2007;**98**:077401
- [45] Johnson BL, Shiao H-H. Guided magneto-plasmon polaritons in thin films: Non-reciprocal propagation and forbidden modes. *Journal of Physics: Condensed Matter*. 2008;**20**(33):335217
- [46] Yu Z et al. One-way electromagnetic waveguide formed at the interface between a plasmonic metal under a static magnetic field and a photonic crystal. *Physical Review Letters*. 2008;**100**:23902

- [47] Hadad Y, Steinberg B. Magnetized spiral chains of plasmonic ellipsoids for one-way optical waveguides. *Physical Review Letters*. 2010;**105**:233904
- [48] Lan Y-C, Chen C-M. Long-range surface magnetoplasmon on thin plasmon films in the Voigt configuration. *Optics Express*. 2010;**18**(12):12470
- [49] Khanikaev A et al. One-way extraordinary optical transmission and nonreciprocal spoof plasmons. *Physical Review Letters*. 2010;**105**:126804
- [50] Ferreira-Vila E et al. Intertwined magneto-optical and plasmonic effects in Ag/Co/Ag layered structures. *Physical Review B*. 2009;**80**:125132
- [51] Drezdzon SM, Yoshie T. On-chip waveguide isolator based on bismuth iron garnet operating via nonreciprocal single-mode cutoff. *Optics Express*. 2009;**17**(11):9276-9281
- [52] Temnov V et al. Active magneto-plasmonics in hybrid metal-ferromagnet structures. *Nature Photonics*. 2010;**4**(February):107-111
- [53] Torrado JF et al. Magneto-optical effects in interacting localized and propagating surface plasmon modes. *Optics Express*. 2010;**18**(15):15635-15642
- [54] Zhu H, Jiang C. Nonreciprocal extraordinary optical transmission through subwavelength slits in metallic film. *Optics Letters*. 2011;**36**(8):1308-1310
- [55] Belotelov VI et al. Enhanced magneto-optical effects in magnetoplasmonic crystals. *Nature Nanotechnology*. 2011;**6**(6):370-376
- [56] Ferreira-Vila E et al. Magneto-optical and magnetoplasmonic properties of epitaxial and polycrystalline Au/Fe/Au trilayers. *Physical Review B*. 2011;**83**:205120
- [57] Bonanni V et al. Designer magnetoplasmonics with nickel nanoferrromagnets. *Nano Letters*. 2011;**11**:5333-5338
- [58] Lan Y-C, Chang Y-C, Lee P-H. Manipulation of tunneling frequencies using magnetic fields for resonant tunneling effects of surface plasmons. *Applied Physics Letters*. 2007;**90**(17):171114
- [59] Kong F et al. Analysis of the surface Magnetoplasmon modes in the semiconductor slit waveguide at terahertz frequencies. *Progress in Electromagnetics Research*. 2008;**82**: 257-270
- [60] Hu B et al. Optical transmission resonances tuned by external static magnetic field in an n-doped semiconductor grating with subwavelength slits. *Optics Communications*. 2008;**281**(24):6120-6123
- [61] Liu X-X et al. Dispersion mechanism of surface magnetoplasmons in periodic layered structures. *Applied Optics*. 2009;**48**(16):3102-3107
- [62] Liu Z, Jin G. Extraordinary THz transmission through subwavelength semiconductor slits under antiparallel external magnetic fields. *Applied Physics A*. 2011;**105**(4):819-825

- [63] Hu B, Wang QJ, Zhang Y. Slowing down terahertz waves with tunable group velocities in a broad frequency range by surface magneto plasmons. *Optics Express*. 2012;**20**(9): 10071-10076
- [64] Hu B, Wang QJ, Zhang Y. Broadly tunable one-way terahertz plasmonic waveguide based on nonreciprocal surface magneto plasmons. *Optics Letters*. 2012;**37**(11):1895-1897
- [65] Hu B et al. Active focal length control of terahertz slitted plane lenses by magneto-plasmons. *Plasmonics*. 2011 published on line: <http://www.springerlink.com/content/p531745636224004/>
- [66] Chen J et al. Efficient unidirectional generation of surface plasmon polaritons with asymmetric single-nanoslit. *Applied Physics Letters*. 2010;**97**(4):041113
- [67] Williams CR et al. Highly confined guiding of terahertz surface plasmon polaritons on structured metal surfaces. *Nature Photonics*. 2008;**2**(3):175-179
- [68] Hau LV et al. Light speed reduction to 17 metres per second in an ultracold atomic gas. *Nature*. 1999;**397**(6720):594-598
- [69] Sandtke M, Kuipers L. Slow guided surface plasmons at telecom frequencies. *Nature Photonics*. 2007;**1**(10):573-576
- [70] Fitrakis E, Kamalakis T, Sphicopoulos T. Slow light in insulator-metal-insulator plasmonic waveguides. *Journal of the Optical Society of America B*. 2011;**28**(9):2159-2164
- [71] Fitrakis E, Kamalakis T, Sphicopoulos T. Slow-light dark solitons in insulator-insulator-metal plasmonic waveguides. *Journal of the Optical Society of America B*. 2010;**27**(9): 1701-1706
- [72] Yu N et al. Designer spoof surface plasmon structures collimate terahertz laser beams. *Nature Materials*. 2010;**9**(9):730-735
- [73] Verslegers L et al. Planar lenses based on nanoscale slit arrays in a metallic film. *Nano Letters*. 2009;**9**(1):235-238
- [74] Hu B, Wang QJ, Zhang Y. Systematic study of planar plasmonic slit lenses and the focal shift effect. *Nanotechnology*. 2012;**23**(44):444002